Meteoritics & Planetary Science 41, Nr 2, 285–304 (2006)
Abstract available online at http://meteoritics.org

Stratigraphy and composition of lava flows in Mare Nubium and Mare Cognitum

Roberto BUGIOLACCHI[1*], Paul D. SPUDIS[2], and John E. GUEST[3]

[1]Department of Earth Science, University College London, London, UK
[2]Applied Physics Laboratory, Johns Hopkins University, Laurel, Maryland, USA
[3]Department of Earth Science, University College London, London, UK
[*]Corresponding author. E-mail: bugiolacchi@hotmail.com

(Received 15 September 2004; revision accepted 18 November 2005)

Abstract–Three major periods of basaltic activity characterize the infill of the basins. Each of these periods was itself punctuated by discrete phases of widespread magma eruptions: three during both the Late Imbrian Epoch and the early Eratosthenian Period and then two in the late Eratosthenian Period. We found the youngest lavas off the eastern border of the Fra Mauro peninsula and, mantling a much larger area, over most of the central western Nubium basin.

Our results place the Nubium/Cognitum basalts in the low-Ti category (1–5 wt% TiO_2).

The data indicate that the majority (~90%) of the mare terrain has iron content between 18 and 22 wt%. In particular, FeO contents tend to concentrate toward two compositional poles, each of ~20 wt%, and a much smaller one of ~15 wt%. These values are typical of nearside lunar maria.

To complement our compositional data, we present a census of craters larger than 500 m using Orbiter IV images. The result was a crater count average with frequency 5.6×10^{-2} km^{-2}, translating into an inferred mean age of 3300 Ma for the exposed lava flows.

By combining lava chemistry with age, we find a possible correlation between the ages of the most prominent flow units and their estimated titanium content, with younger basalts becoming progressively Ti-richer with time (from 2–3 to 4–5 wt% TiO_2).

INTRODUCTION

Overview

Remote sensing of the lunar maria has allowed us to investigate subtle color differences among lunar soils, and in particular, regions where the maria appear uniform have been shown to exhibit a range of mineral compositions with differences large enough to suggest distinctive basaltic flows. This method has become another tool to help us study the three-dimensional geology of the maria.

The aim of this work is to investigate the stratigraphy and composition of Mare Nubium and Mare Cognitum by combining data on the geographical distribution of the elements iron and titanium within the maria, relative and estimated dating of each potential unit, and volumetric estimate of emplacement. Ultimately, work of this type will help advance our understanding of the lunar petrogenesis and maria emplacement.

General Description of the Area

The area covered by this study is a quadrangle centered around the Fra Mauro peninsula, with 908.6 km sides and coordinates 0° to 30.0°S and 2.0° to 32.0°W (Fig. 1). We calculated that maria overlays about 60% of the region, or approximately 500,000 km^2. This area represents the southern edge of Mare Insularum, south of crater Lansberg, Mare Cognitum in the northeast and Mare Nubium in the south; larger craters within the mare are Bullialdus, König, and Birt, plus the surface remnants of, among others, craters Kies, Wolf, Opelt, Lubiniezky, and Lassell.

This region is also characterized by a north-south aligned peninsula containing the plains Fra Mauro, Parry, Bonpland, and Guericke. Other noteworthy geological features are the Rima Hesiodus in the southwest and Rima Flammarion in the northeast. The Rupes Recta (also called Straight Wall) in the southeast is a 120 km long scarp that averages 300 m in height (De Hon 1977). Monte Riphaeus delineates Mare Cognitum on its northwestern boundary.

Geographically, the pre-Nectarian Nubium basin covers nearly two-thirds of the area, centered at 21.3° S, 16.6° W, and it represents one of the most ancient circular basins on the Moon, with a diameter of about 750 km (Stuart-Alexander and Howard 1970). Nevertheless, there is clear evidence that the basin did not form by a single large impact. In fact, the

© The Meteoritical Society, 2006. Printed in USA.

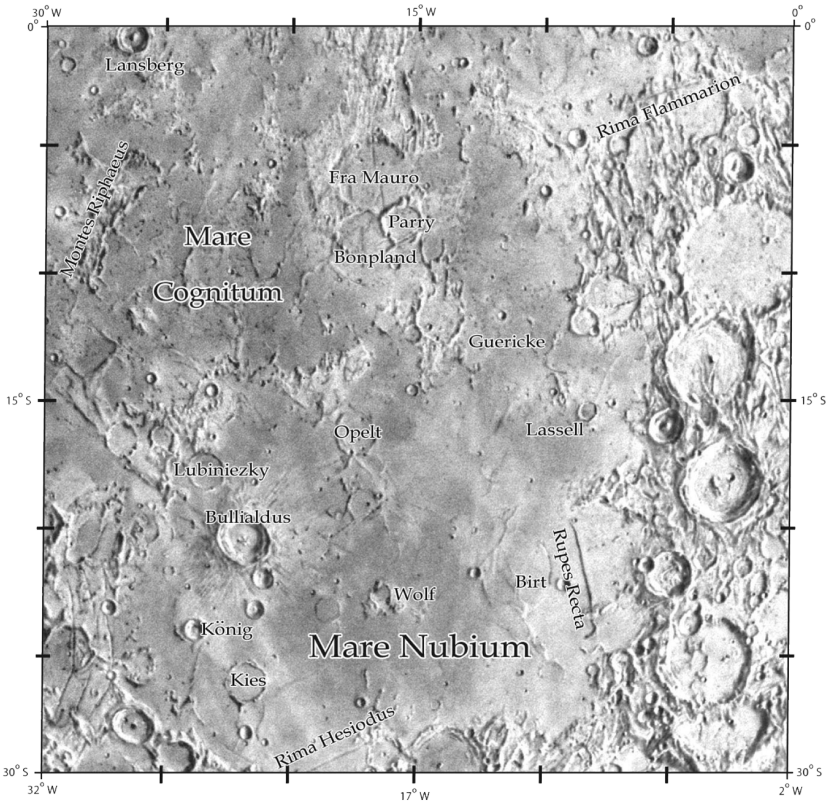

Fig. 1. Map of the region under study (MAP I-2276, National Aeronautics and Space Administration, 1992).

surviving morphology of at least four major basin rings is still clearly visible (De Hon 1977; Hawke and Head 1977).

The mountain range Montes Riphaeus to the northwest of Mare Cognitum (10.0°S, 23.1°W) may represent what is left of the rim crest that defined the 376 km impact basin. Hawke and Head (1977) proposed a combination of three large impacts (north Riphaeus, Cognitum, and east Cognitum), with Cognitum the largest (D = 230 km), as the principal constituents of the present morphology.

METHODS

The Technique of Remote Sensing UVVIS-IR Applied to Lunar Soils

Objects ranging in size from tens of kilometers to less than one micron have battered the lunar surface since its formation some 4.5 Ga ago. This has produced a layer of shattered rocks and fine debris called regolith (McKay et al. 1991), which covers most of the lunar surface. The bulk of it consists of particles smaller than one centimeter in size (Heiken 1975; Houck 1982)

Regolith is 3–8 m deep in the maria (Moore et al. 1980; Taylor 1982; Hörz et al. 1991) but may be up to 15 m deep in older highland regions (Langevin and Arnold 1977; McKay et al. 1991). What we see of the lunar surface is the top layer of this mixed, pulverized, and reworked veneer of ancient crystalline rocks, breccias, glasses, minerals, and agglutinates. The topmost regolith (in the region of a few centimeters) is also matured and saturated by solar wind particles.

Generally, differences in brightness of the lunar soil are due to the reflectance properties of those materials with higher plagioclase feldspar content (higher albedo) compared to those rich in mafic minerals (lower albedo). Concurrently, the continuous exposure to space weathering, mainly in the form of micrometeorite bombardment, solar wind particles, and galactic cosmic rays modify the reflectance properties of the lunar soil with time (Pieters et al. 1993). Depositional products such as agglutinated impact materials, sputter deposits, and impact-derived vapors (Keller et al. 1999) combine in altering the lunar surface's optical characteristics.

Remote sensing of the lunar surface relies on the assumption that regolith is geochemically representative of the underlying bedrock. Much research has gone into proving this connection ever since the first samples were brought back to Earth (Oberbeck et al. 1973). On average, only about 5% of the regolith comes from distances beyond a 100 km radius and 50% from less than 3 km (Gault et al. 1974; Taylor 1975). The bulk of highlands debris in mare regolith has been estimated to originate directly from beneath relatively thin mare flows, derived dominantly by vertical mixing (Rhodes 1977; Hörz 1978). Nevertheless, more recent studies (e.g., Mustard and Head 1996; Staid and Pieters 2000; Li and

Table 1. Clementine UVVIS instrument parameters (an additional broad band filter was available on the filter wheel). Compiled using data from Nozette (1994).

Filter	Band center ± 1σ
A	415 ± 20 nm
B	750 ± 5 nm
C	900 ± 15 nm
D	950 ± 15 nm
E	1000 ± 15 nm

Table 2. Comparison between the visible spectrum values for the three fundamental colors and the assigned RGB colors.

Color	Real approximate wavelength ranges (nm)	Assigned controlling bandpass filters (nm)
Red	740–620	950 (NIR) filter D
Green	575–500	750 (red) filter B
Blue	500–445	415 (UV) filter A

Mustard 2000) have re-evaluated the importance of lateral mixing in the distribution of materials on the lunar surface.

Since the depth of penetration for reflected visible–near-infrared (VIS-NIR) energy is just a few microns, only the uppermost surface material is characterized by the observed spectrum. The optical properties of this layer are dominated by the finer fractions (<10 μm) (Pieters et al. 1993; Keller et al. 1998), which, while composing only about 10–20% of the regolith by weight, constitute about two-thirds of the surface area (Housley 1980). In mature regolith, major contributors to reflectance variations in these fractions are the size and distribution of the nanophase metal iron (Fe^0) in the soil grains (Keller et al. 1998, 2000; Noble et al. 2000).

A complex history of basalt petrogenesis and mare volcanism has shaped the present lunar maria. Establishing the relative abundances of mafic minerals such as olivine, pyroxene, and ilmenite is instrumental in establishing this history. These can be estimated by obtaining the bulk oxide content in the regolith, dominated by SiO_2, FeO, TiO_2, Al_2O_3, MgO, and CaO (Papike et al. 1991). The abundances of mafic minerals vary across the maria due to lateral differences in magma source regions and fractionation histories (Campbell et al. 1997). Most of the information on composition and maturity of the regolith comes from spectrophotometric observations and orbital geochemistry data that have been calibrated according to measured values for the Apollo and Luna landing sites (Campbell et al. 1997).

To summarize, three factors control the spectral reflectance of the lunar surface: soil maturity, bedrock mineralogy, and the degree of contamination by exotic impact debris. The means by which we interpret the relative contribution of each is described next.

Data Sources for the Study

Building on a number of methodologies that have been developed in the last three decades (e.g., Whitaker 1972a; McCord and Adams 1973; Charette et al. 1974; Hapke et al. 1975; Pieters 1978; Johnson et al. 1991; Pieters et al. 1993; Melendrez et al. 1994; Fischer and Pieters 1996), Lucey et al. (1995, 1996, 1998, 2000) utilized data from the Clementine ultraviolet-visible (UVVIS) camera (e.g., Nozette et al. 1994; Pieters et al. 1994) mission's 415, 750, and 950 nm filters to estimate TiO_2 and FeO abundances.

The bulk of the surface mapping by Clementine was based on observations from the approximate local zenith (Kresalvsky et al. 2000). Among several other scientific instruments, the satellite carried UVVIS multispectral cameras. These allowed, by means of suitably chosen filters, the collection of reflected solar radiation in five discrete wavelengths (see Table 1). The spectral bandpasses focused on those parts of the spectrum affected by both composition variation and maturity of the regolith (Pieters et al. 1994).

The Clementine raw data, traditionally called engineering data records (EDR) (Eliason et al. 1995), was made available by the Planetary Data System (PDS) in cooperation with the Naval Research Laboratory in the form of 88 CD-ROM volumes. The UVVIS digital image model (DIM) was imported into Integrated Software for Imaging Spectrometers (ISIS) (Torson and Becker 1997) running on a Unix/Sun workstation computer. This produced an "image cube" that subsequently underwent a five-step (stages 0 to 4) processing routine designed to minimize inaccuracies, such as radiometric and geometric errors, and normalize the sun-viewing geometry (Eliason 1997; Torson and Becker 1997). The obtained DIM data was finally mosaicked to obtain an image cube in the chosen orthographic projection (Eliason et al. 1999; Isbell et al. 1999; Robinson et al. 1999).

NASA View, a PDS software program display tool supplied by PDS/JPL, can show full-resolution cube images with an average spatial resolution of around 200 meters per pixel. These can either be from a single filter (such as the "albedo" 750 nm image) or multispectral, combined and processed according to a specific algorithm (see Table 2 for individual descriptions).

By making use of the multilevel data potential of cube images, a more basic version of NASA View, called Quick View, was used to extract the absolute location of each interrogated pixel on the Moon (lat/long) along with the estimated iron and titanium abundances. Geographical distances were also determined by exploiting the given absolute location between two points (i.e., pixels), expressed as lines and samples numbers.

Derivation of Band Composite Image

Data from three individual filters were assigned to the RGB spectrum to produce a band composite color map, often called DBA (for filters D, B, and A) (Table 2). The underlying red color of the regolith, displayed as green, contributes to the general greenish undertone of this image. The result is a picture that subtly but significantly emphasizes visible to

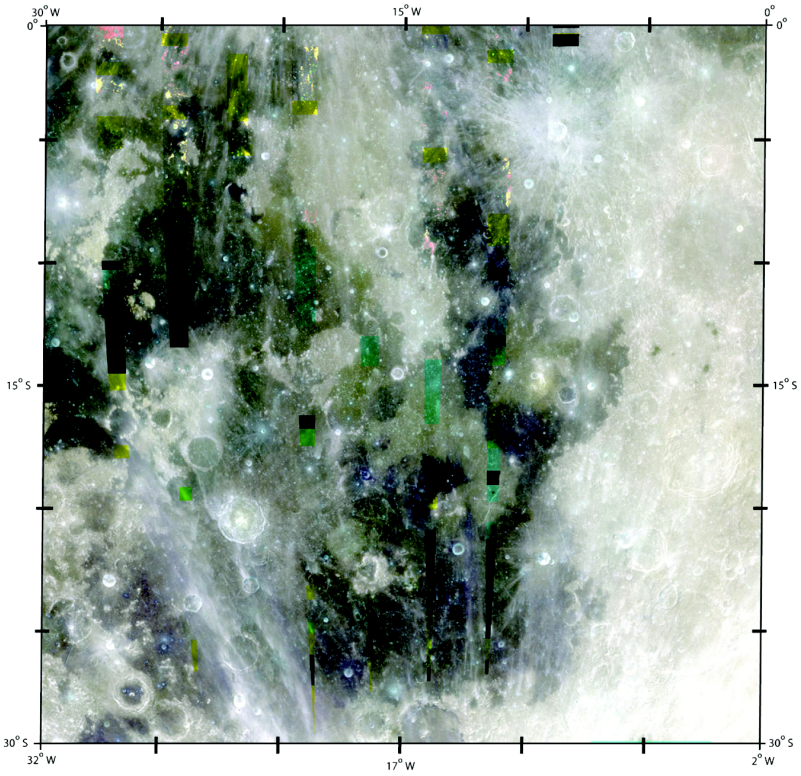

Fig. 2. A band composite image (DBA).

near-infrared color differences of the Moon's surface. Following appropriate brightness threshold filtering and emphasis, we produced an enhanced color image that focuses on the surface's albedo differences in the region (Fig. 2).

Derivation of TiO_2 Maps

One of the principal parameters in classifying the mare basalts sampled at the lunar landing sites is the TiO_2 content (reflecting the abundance of the mineral ilmenite $FeTiO_3$). The composition of the liquid produced by the partial melting of typical terrestrial mantle rocks depends both on the degree and on the conditions of melting, such as pressure, temperature, and volatile content (Hall 1996). Titanium is an important elemental indicator in mare basalt petrogenesis, reflecting the composition and state of the partial melt at depth (Elphic et al. 2001). Generally, higher melting temperatures (and consequent increasing percentage of melting) will yield progressively lower concentrations of TiO_2 in the liquid (e.g., Mysen and Kushiro 1977). Lunar samples demonstrate that titanium content is the major compositional variable among mare basalts (e.g., Whitaker 1972b; BVSP 1981).

Charette et al. (1974) found a correlation between UVVIS color balance and TiO_2. This relation could be understood in view of the work carried out by Hapke et al. (1975) on a model for bidirectional reflectance. He found that opaque minerals, such as ilmenite (the major mineral carrier of TiO_2 and dominant opaque phase) have a strong influence on lunar reflectance. Opaques are by definition dark and their presence therefore decreases the reflectance of an iron-bearing regolith, its spectral contrast, and its spectral slope, in essence making it less red (Lucey et al. 2000).

These findings allowed the construction of the early titanium content maps based on Earth-based multispectral images of the Moon (e.g., McCord and Adams 1973; Pieters and McCord 1976; Johnson et al. 1977; Matson et al. 1977; Pieters 1978). In the following years, many researchers worked on improving and refining the mathematical algorithms (Johnson et al. 1985, 1991; Blewett et al. 1997; Lucey et al. 1998, 2000; Gillis and Jolliff 2001; Gillis et al. 2003, 2004). Others conducted parallel research on the photometric properties of the Moon's surface (e.g., Fisher and Pieters 1996; Shkuratov et al. 1999; Kreslavsky et al. 2000) by experimenting on various lunar samples, adding to the work of the Hawai'ian group (Lucey and co-workers).

The TiO_2 map (Fig. 3) was produced using an updated version of the original algorithm presented by Lucey et al. (1996). It uses measurements of the 415 nm and 750 nm reflectance and, in a simplified way, can be expressed as:

$$\mathrm{wt\%TiO_2} = 3.708 \times \arctan\left\{\frac{(R_{415}/R_{750}) - y_{0Ti}}{R_{750} - x_{0Ti}}\right\}^{5.979}$$

where R_x is the reflectance at wavelength x (nm) and x_{0Ti} and y_{0Ti} represent the origin.

Experimental data has shown on ten direct trials that the

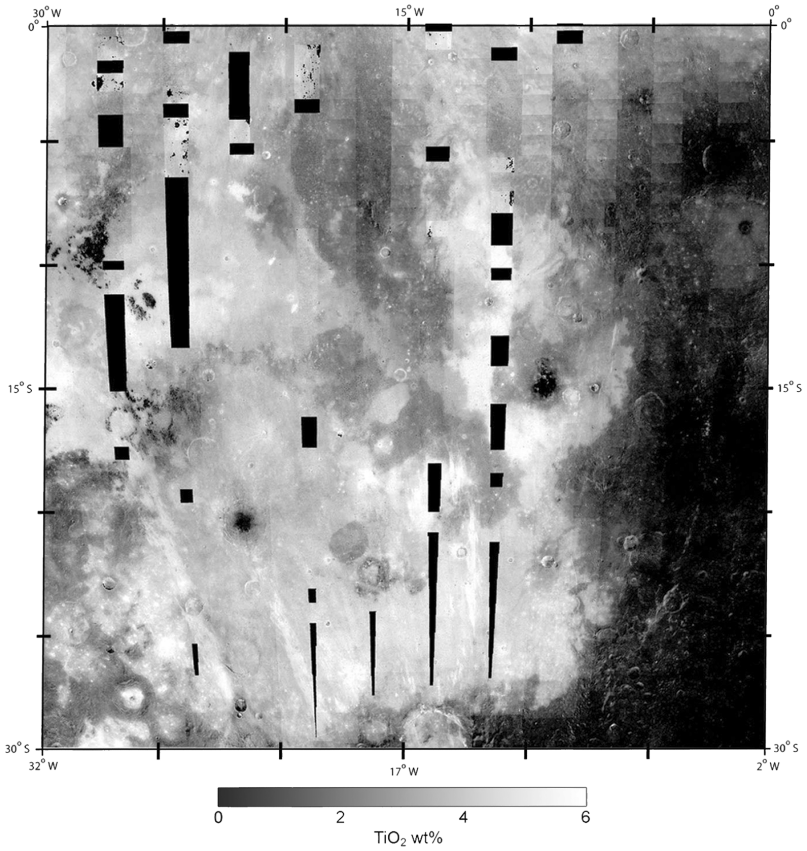

Fig. 3. An image of Nubium showing TiO_2 abundance (brighter = higher%).

average standard deviation of the test set data is 1.00 wt% TiO_2 (Lucey et al. 2000a). This essentially shows that titanium values are directly proportional to the "blueness" of an area and inversely proportional to its reflectance in the red part of the spectrum.

Derivation of FeO Maps

A reduction of ferrous iron (FeO) in glass and minerals to submicrometer particle of native iron (Fe^0) occurs with exposure to the space environment (McKay et al. 1991). As a result, lunar soils tend to darken and redden with time in tandem with other effects of space weathering (Fischer and Pieters 1994, 1996). Lucey et al. (1995) reasoned that a color ratio involving 750 nm reflectance and the far end of the visible spectrum (NIR, 950 nm) would indicate the (ferrous) iron abundance percentage (Fig. 4).

According to Lucey et al. (2000a):

$$\text{wt\%FeO} = \left\{ 17.427 \times \arctan\left[\frac{R_{950}/R_{750} - y_{0Fe}}{[R_{750} - x_{0Fe}]} \right] \right\} - 7.565$$

where R_x is the reflectance at wavelength x(nm) and $x_{0\text{Fe}}$ and $y_{0\text{Fe}}$ represent the origin.

The average standard deviation of the test set data was 1.29 wt% FeO. Effectively, the Lucey method aims to measure the spectral effects of ferrous iron in major lunar minerals such as pyroxene and olivine (Blewett and Hawke 2001).

Derivation of "False Color" Ratio Composite Map

Another type of map, a "false color" ratio composite was also derived from Clementine DIMs (Fig. 5). The use of ratios is to compensate for albedo variations and exaggerate color variations (Belton et al. 1992; Pieters et al. 1994). The resulting multispectral composite mosaic is a much clearer representation of the reflectance characteristics in the region due to variations in regolith maturity and mineralogy. The ratio between images taken using filters at 750 nm and near 1000 nm (750/950 nm) also helps in identifying the presence of fresh mafic minerals in the lunar materials. This is due to the absorption band centered near 1.0 μm resulting from a combination of spectral absorption by Fe^{2+} in clinopyroxene and in olivine (e.g., Hapke et al. 1975). Table 3 shows the ratio controlling the RGB values.

DATING THE SURFACE

We investigated Maria Nubium and Cognitum lunar basalt ages by calculating the crater size-frequency distribution for craters down to 500 m in diameter (for a full

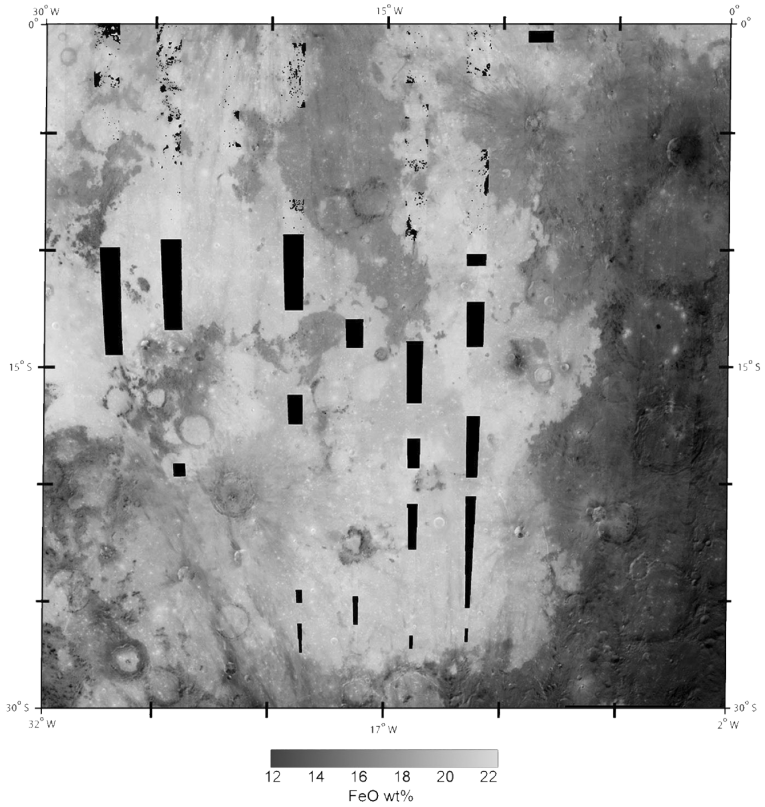

Fig. 4. An image of Nubium showing FeO abundance (brighter = higher%).

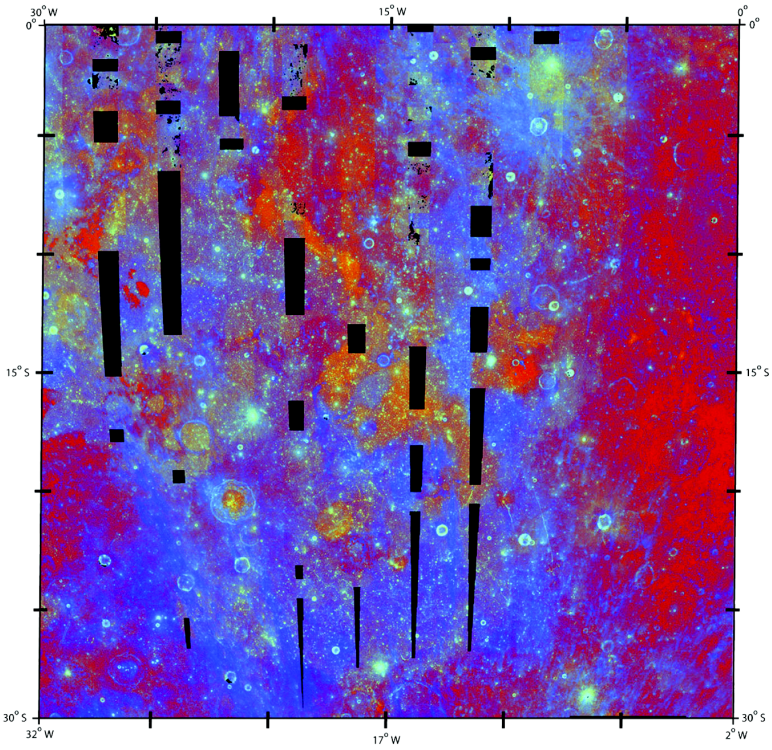

Fig. 5. A color-ratio composite of Nubium from ultraviolet and visible (UV-VIS) mosaic in three spectral bands.

Table 3. The ratios controlling the RGB values.

Color	Ratios (nm)
Red	750/415
Green	750/1000 or 750/950
Blue	415/750

account of methodology and background, see Hiesinger et al. 2000). Clementine data could not be used for this part of the research due to both the relatively low resolution of its UVVIS camera (~200 m/px) (Nozette et al. 1994) and, crucially, the low-phase angle of the images; these factors combined in making it difficult to discern craters <1 km in diameter. Instead, we used images from the 1967 Lunar Orbiter IV mission, which have spatial resolutions between 60–150 m, an incidence angle of 10–30°, and sharper contrast.

Each photographic print was first scanned at high resolution and imported into a professional image manipulation application. Substantial tonal range adjustments were required in order to level extremes in the contrast/luminosity characteristics. We counted nearly 10,000 craters larger than 500 m scattered over a sampled mare surface of 225,000 km^2.

We encountered several limitations and uncertainties in our method as the work of spotting suitable craters progressed. Some small sections of the original Orbiter images were overexposed and suffered from poor contrast resolution. In addition, when viewed in high resolution, some areas displayed what appeared to be film-developing "blotches." It is also probable that a few volcanic features, such as domes and cones, as well as naturally occurring terrain depressions, were interpreted as craters and included in the count. Nevertheless, the potential errors represent only a tiny percentage of the total crater census. A far trickier task was the differentiation between primary and secondary impact craters. A low-resolution inspection of each area was deemed sufficient to estimate and approximate the extent of the "contamination." An arbitrary lower crater count was applied for the given area.

Neukum (1975a) estimated the systematic uncertainty of the standard distribution curve to be <10% for 0.8 km ≤ D ≥ 3 km, and higher percentages as the diameter of the sampled craters increases. Furthermore, crater densities relative to lunar maria average and Apollo missions are assumed with a 10% uncertainty (Table 8.4.2 in BVSP 1981). As a result, we took an error of ten percent to be our upper limit of uncertainties for this part of our work.

Converting the crater count per square kilometer into an indication of model age requires statistical records on subkilometer crater populations plus reliably dated and geographically pertinent rock samples. Most lunar crater chronology is based on statistical records of impacts larger than one kilometer in diameter (e.g., Arvidson et al. 1976; Hiesinger et al. 2000; Tables 8.4.1 and 8.4.2 from BVSP 1981) in the geographical proximities of the few directly sampled areas of the Moon (Apollos 11–17, Luna 16, and Luna 24). We produced Fig. 6 from a number of data sources (Tables 8.4.1 and 8.4.2 from BVSP 1981; Shultz and Spudis 1983).

THICKNESS OF UNITS

There has been much research into the dynamics of high-velocity impacts. Melosh (1989) suggested an approximate relationship of 1/10 between the depth of excavation and the diameter of the transient crater for simple craters (≤14 km on the Moon) (Pike 1974). These results were confirmed by later studies (e.g., Spudis 1993; Grieve and Pilkington 1996). At this scale, the final crater diameter is a good approximation of the transient excavation.

Crater ejecta reflect the composition of the excavated target. If an impact penetrates the maria down to the highland bedrock, we would expect the ejecta blanket to contain a proportion of highland material. Indeed, a reversed stratigraphy characterizes the geology of a crater rim: the deepest excavated material is emplaced to form the crater rim (Stöffler et al. 1975; Shoemaker 1977; Melosh 1989; Budney and Lucey 1998). Using the UVVIS Clementine data set, we are able to differentiate between these two types of ejecta through their different iron values. Fe-poor highland material, mixed with the more iron-rich local basalts, will result in the darkening of part of the ejecta blanket nearer to the crater rim (as viewed in the iron map). The degree of admixing of subsurface highland material with mare basalts is a function of the depth of excavation and contamination (after Thomson et al. 1998):

$$\frac{Ch}{Mh} = \frac{FCE - H}{E - H} \quad (1)$$

where *Ch* is the maximum excavation depth (m), *Mh* is the estimated maria depth (m), *FCE* is fresh crater ejecta, i.e., pristine mare basalt (FeO wt%), *E* is dark mix material, i.e., mare + highland bedrock (FeO wt%), and *H* is the nearest highland material (FeO wt%).

We obtained accurate crater diameter measurements from the same image cubes used to determine FeO wt%. We rearranged the equation to find the estimated maria depth in meters:

$$Mh = Ch\frac{E - H}{FCE - H} \quad (2)$$

RESULTS

Mineralogy

TiO_2 Results

Analysis of lunar rock samples initially suggested a strongly bimodal distribution of titanium in mare basalts,

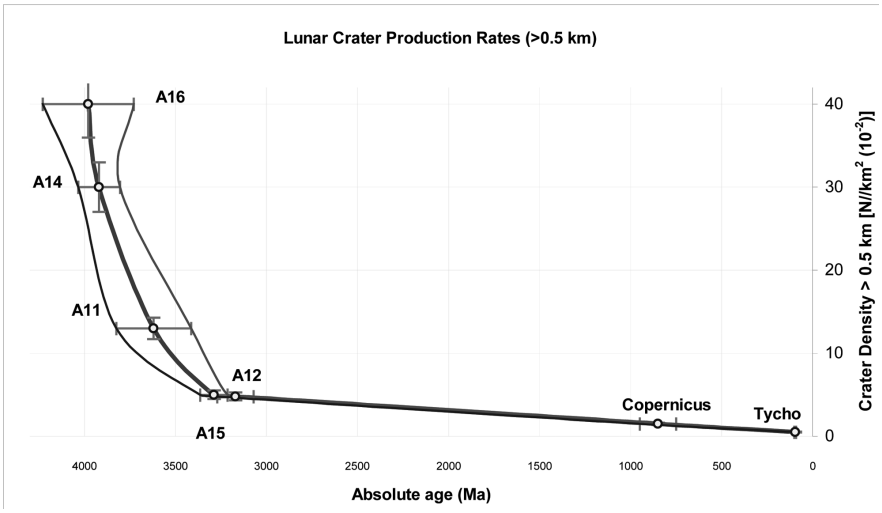

Fig. 6. A graph showing the relation between crater density and age of surface (based on Tables 8.8.1, 8.4.1, and 8.4.2 from BVSP 1981; Shultz and Spudis 1983).

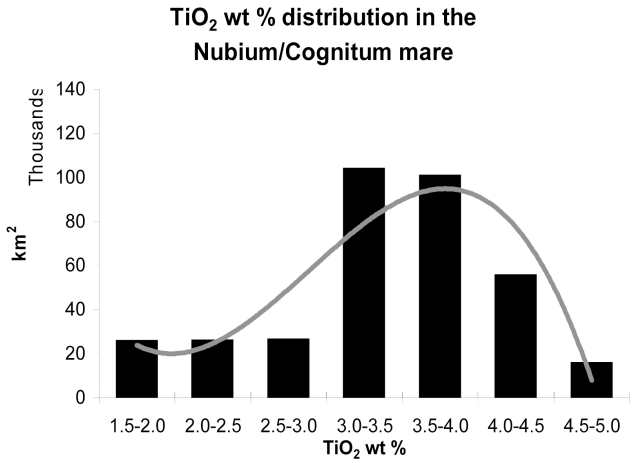

Fig. 7. Histograms of TiO_2 wt% distribution in the Nubium/Cognitum mare.

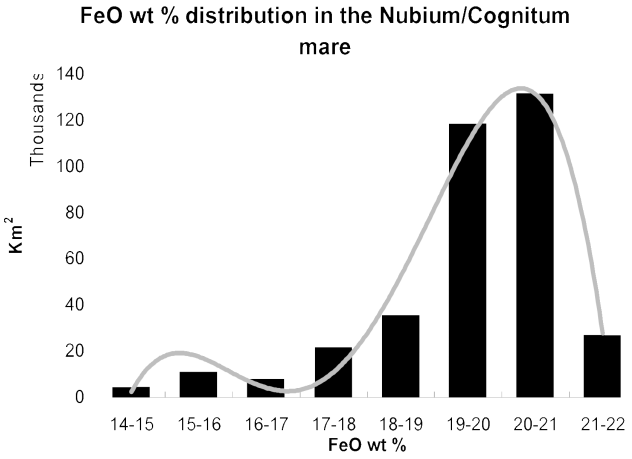

Fig. 8. Histograms of FeO wt% distribution in the Nubium/Cognitum mare.

with most material averaging ~2.5–3 wt% TiO_2 and, in a far less significant proportion, 12–13 wt%. Later studies of multispectral data from Earth-based observations and various remote-sensing missions (mostly Galileo, Clementine, and Prospector), instead have found a continuous gradation from very low-Ti to high-Ti mare basalts (e.g., Giguere et al. 2000).

Our results place the Nubium/Cognitum basalts in the low-Ti category (1–5 wt% TiO_2), with nearly 80% of the data in the range of 3–5 wt% (Fig. 7). These values should be shifted upward (~20%, according to Giguere et al. 2000) because of admixing and "contamination" of the maria regolith with materials excavated or ejected from underlying and neighboring highland rocks. Taking these adjustments into account, our figures are still comparable with samples of low-Ti basalts and the inferred unimodal trend.

FeO Results

Hand specimens of low-titanium lunar basalts average ~20.2 wt% FeO (Jolliff et al. 2000). Multispectral Clementine data indicate that the majority (~90%) of the mare terrain under investigation have an iron content between 18 and 22 wt%. In particular, FeO variances tend to concentrate toward two compositional poles, each of ~20%, and a much smaller one of ~15 wt% (Fig. 8). The latter low FeO concentration in the soil is probably due to soil "contamination" by horizontal and/or vertical admixing with iron-poor highland material.

Surface Ages

Our crater count averages a frequency of 5.6×10^{-2}/km^2 for craters larger than 500 m in diameter. This translates into

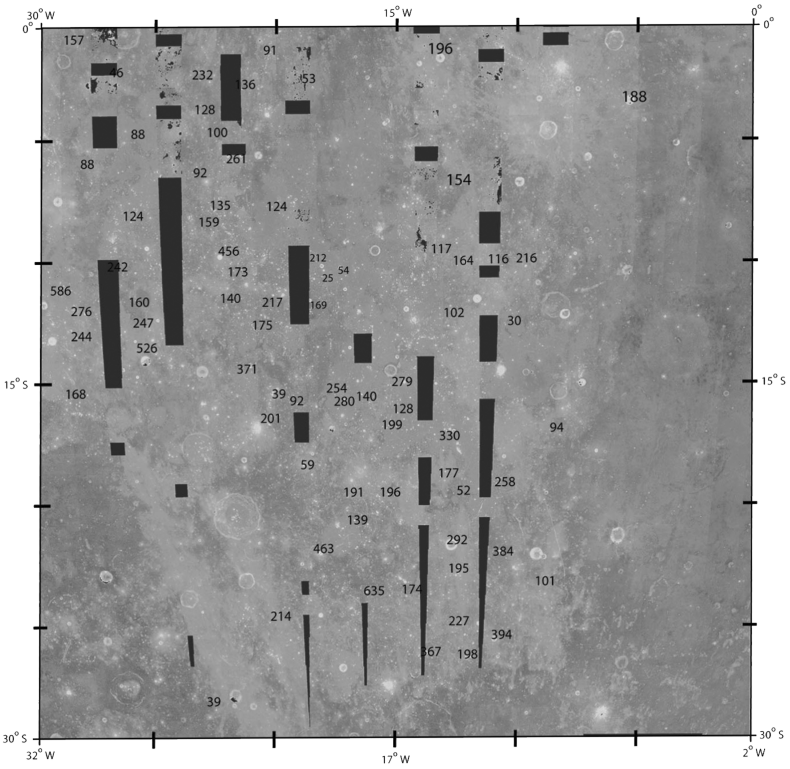

Fig. 9. A map of inferred mare thickness (m).

an inferred mean age of 3300 Ma for the majority of the exposed lava flows. Ages range between 2340 (±400) Ma and 3550 (±80) Ma. Due to the uncertainties and approximations used in extrapolating ages expressed in years from crater count statistics (Fig. 6), we used the latter as a more objective comparative tool.

Unit Thicknesses

Only a fraction of the 74 craters we investigated actually feature a distinctively low-FeO ejecta ring. We decided to supplement our data with values from craters that showed a relatively dark (as in the iron map) crater floor. Their interpreted lower iron content could be a consequence of the presence of highland material within the allochthonous breccia. Figure 9 shows the inferred mare depths. It is clear that, due to both the paucity of the data and the uncertainties in measuring crater floors' compositions, we need to be cautious about the reliability of the results.

Our results broadly agree with previous studies on maria thickness variations (De Hon 1977): a possible thickening of the basalt layers in the center of the Nubium basin (~17°W, 23°S), the northern eastern region (~10°W, 20°S), and the northern border (~18°W, 17°S). We are also reporting two areas of mare thickening in Mare Cognitum: one just north of Darney D (27.0°W, 14.5°S) and another near the middle of the basin (23°W, 10°S).

ANALYSIS

Stratigraphy

The DBA and false color images, along with the titanium and iron maps, were processed, resized, and printed out as square reproductions of 60.57 cm sides (at a scale of 1:1,500,000).

We also scanned, scaled, mosaicked, and printed Orbiter IV photographs (OIV 132, 125, 120, 108, and 113) and various other sources (i.e., Consolidated Lunar Atlas, Kuiper et al. 1967) to match the scale of the Clementine images as closely as possible.

Figure 10 represents a draft map of potential flow units, constructed through the gathering and comparison of traced albedo and hue differences within each Clementine image. They are numbered accordingly to the sampling sequence. Also displayed are uplands (black), mature and contaminated mare (very dark gray), major craters (dark gray circles), and ejecta blankets (gray).

We produced Fig. 11 by comparing and grouping differences in compositions into nine distinctive geochemical "families." It is important to note that the terms "high-Ti" and "low-Fe" are defined in comparison to the local maria compositional average and not the range of planetary values.

A degree of correlation between age and composition of the regolith can be found in our combined data.

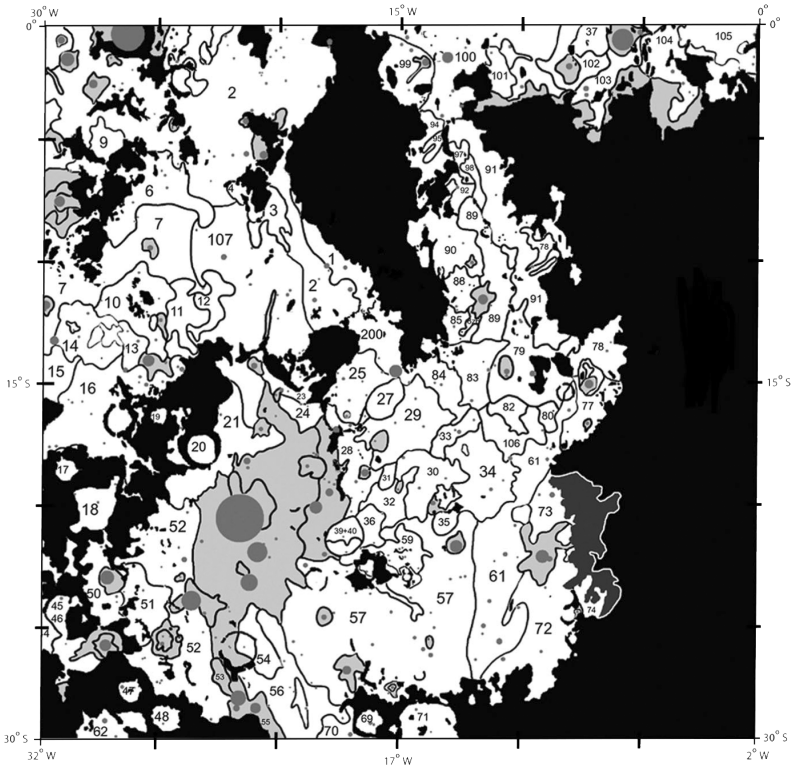

Fig. 10. A map showing individual lava flows in the Nubium region. Also displayed: uplands (black), possible ancient mare (very dark gray), major craters (dark gray circles), and ejecta blankets (gray).

Figures 12 and 13 display the age trend for each group (relatively high-Ti, medium-Ti, and low-Ti). According to our data, it is clear that more heavily cratered terrains are also less Ti-rich. In contrast, our data shows only a weak relationship between iron abundances and age differences of the average units (Figs. 14 and 15). There is a strong possibility that even this slight trend might be the result of contamination from Fe-poor materials from the neighboring highlands, pointing to a general uniform FeO wt% content in the basin's basalts (~19–20%).

Table 4 allows us to compare both the chemical make-up and modeled age among all units (based on classification in Fig. 11). We present two further and progressive levels of amalgamation. Table 5 groups all "original units" (as per Table 4) that have very similar chemical compositions and inferred age.

Geological Map

We produced further merging and subgrouping of the seventeen units into eight potential geological types within the maria (a–h in Table 6). Some minor areas were not included in this final classification: units 16, 7, and 5 are too small, marginal, and too close to either highlands or major craters to be representative of the overall compositional and age trend of the studied area. The soils represented by unit 12 show instead a typical composition of terrains grouped as "e," but they are also characterized by a much more cratered morphology and hence interpreted as older. Nevertheless, all of these four groups were "associate" with their relevant chemical/age group, reflecting our relative reliability bias toward chemical data. We plotted the TiO_2 data and age estimates from Table 6 to produce Fig. 16. The best-fit line confirms our previous findings (Figs. 12 and 13) of a possible trend of soil enrichment in titanium with time. These results agree with other works that found regional trends toward more titaniferous basalts with time (e.g., Hawke et al. 2005), including the last major phases of volcanism within the Imbrium basin (e.g., Staid et al. 1996; Staid and Pieters 2001). Nevertheless, other researchers failed to identify a global trend in titanium variations throughout the infill history of the Moon (e.g., Hiesinger et al. 2001).

Figure 17, which is derived from the crater frequency and TiO_2 data in Table 6, suggests three possible eruptive phases with increasing titanium concentration in the magma with time. This relationship is less clear when modeled ages are considered (Fig. 16). This is probably due to the progressive crater saturation of the lunar surface, believed to increase exponentially for soils older than ~3300 Ma (or ~5.0×10^{-2} 500 km craters per km^2). Table 7 lists the proposed three major eruptive phases in the Nubium/Cognitum region.

Each family group represents distinct periods dating from the Late Imbrian Epoch (I) through the early

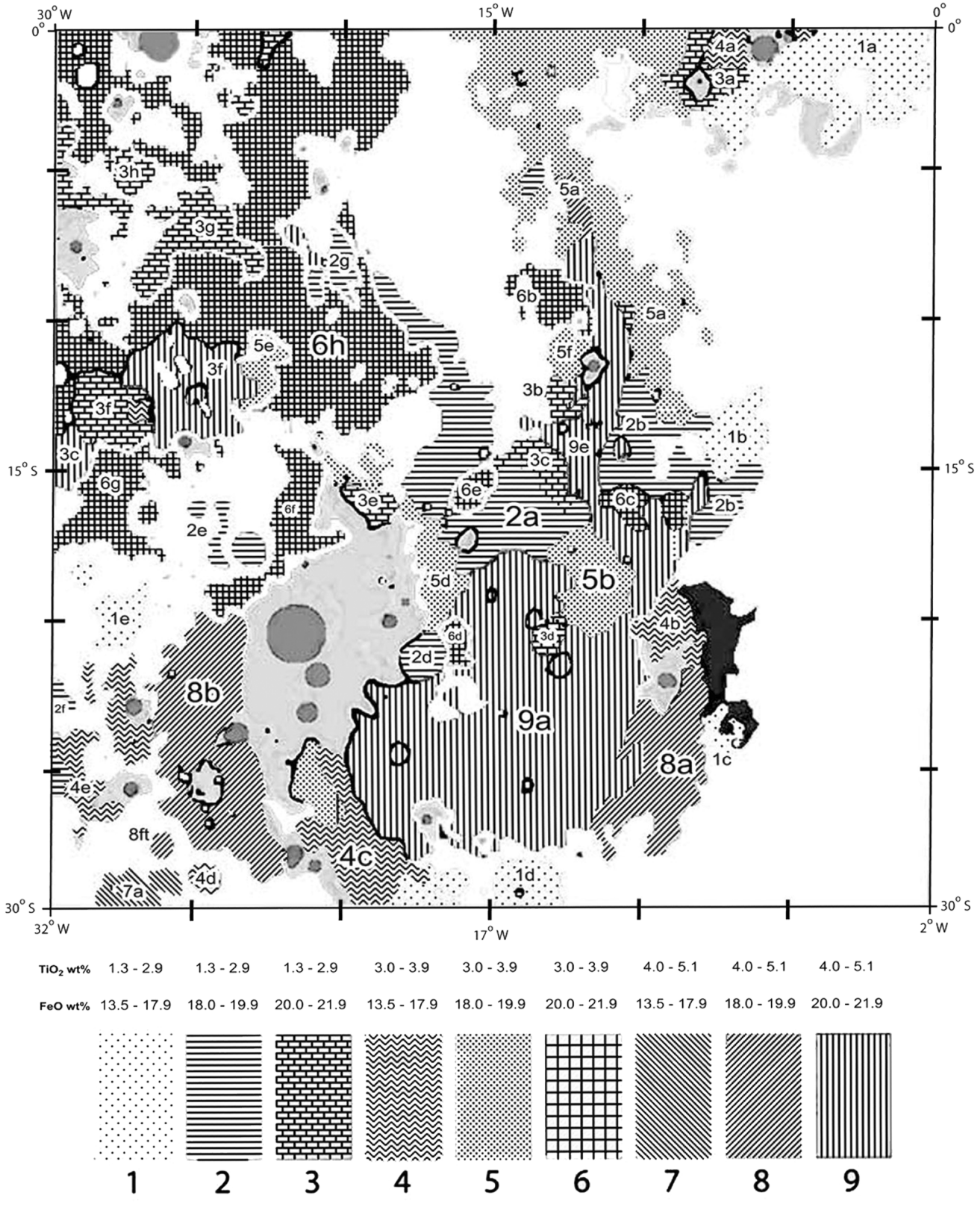

Fig. 11. A map showing the composition of individual lava units.

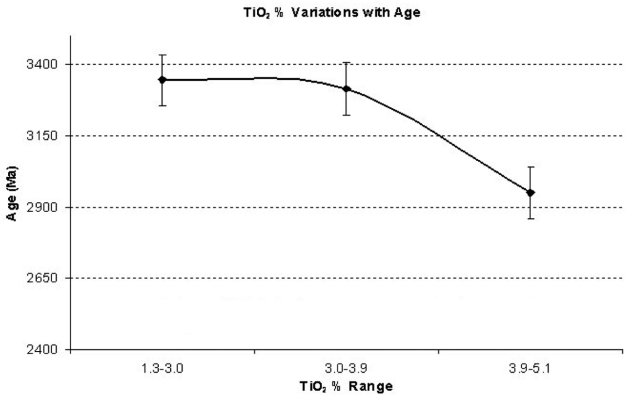

Fig. 12. A graph of TiO_2 wt% variations with age.

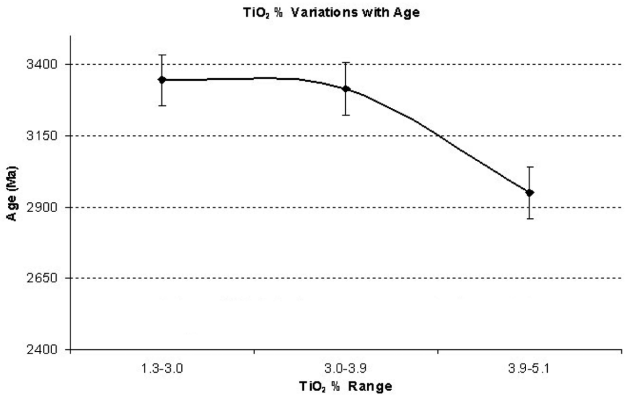

Fig. 13. A graph of TiO_2 wt% variation with crater frequency.

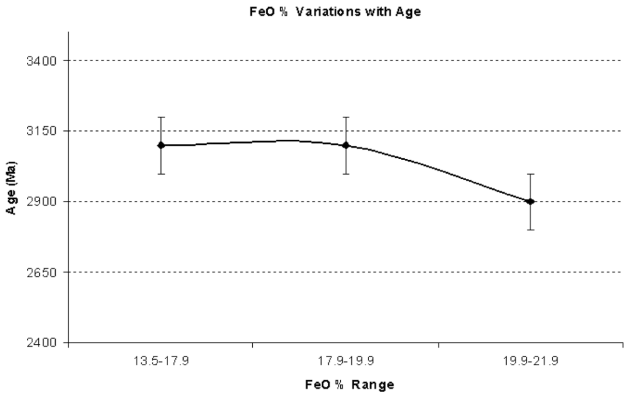

Fig. 14. A graph of FeO wt% variations with age.

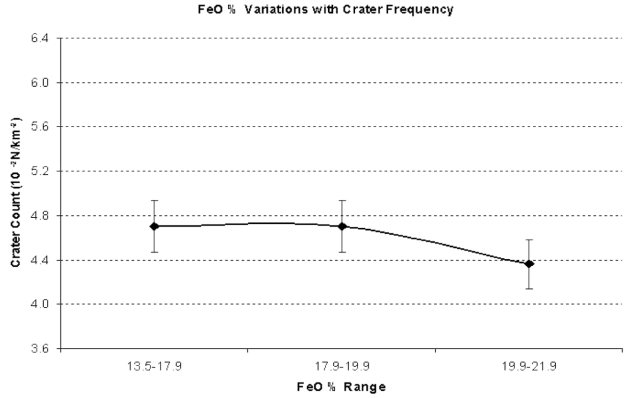

Fig. 15. A graph of FeO wt% variation with crater frequency.

Eratosthenian Period (II) and late Eratosthenian Period (III). Fig. 18 illustrates the geographical distribution of these three families.

All of the data and interpretation gathered in this work is summarized in Fig. 19, a geological map of the lunar quadrangle. It shows nine types of exposed mare basalts, igneous centers and associated flow units, surface morphologies such as ridges, rilles, and faults, numerous impacts that occurred before, during, or after mare emplacements, and ejecta materials from various sources. Note that we are observing only the geologically visible units and using them to interpret the stratigraphy of the maria. Most of these regoliths types may represent only the last of many effusive phenomena witnessed within a given geographical area. We have also to consider contamination from highland materials, especially near the "continental shelves" (i.e., for units "a" and "d"), ejecta from local impacts (units near to "y"), local chemical anomalies (i.e., "j" at 7°S, 22°W), and the general inherent difficulty in acquiring reliable crater frequency data for small geographical areas.

Mare units marked "x" are considered to be remnants the oldest exposed basaltic flows in the region. We find them mostly in embayed coastal areas and show compositions similar to the neighboring highlands. Due to the effects of billion of years of erosion plus substantial vertical and horizontal admixing with non-mare material, the multispectral analysis techniques used in this study cannot offer reliable chemical data of the original basaltic composition.

History of the Area

We inferred a chronological order of the potential flows based on statistical analysis of individual cratering frequency and distribution characteristics. Our dating results are in broad agreement with previous studies of the region (i.e., Wilhelms and McCauley 1971; Boyce 1975), but they are now associated and compared with analysis of surface compositions using Clementine multispectral data. Hiesinger et al. (2003) conducted a similar study of this region with emphasis on the dating of potential flow units. Our results differ substantially on the absolute modeled age of certain key areas (e.g., units "g" and "h"), albeit with better agreement on the relative age of the exposed unit flows.

We find the most ancient and degraded maria ("x" in Fig. 19) either next to terra or within ancient craters (Fra

Table 4. Chemical and cratering data for similar unit flows including age estimates.

Units (new)	Crater density (10^{-2}N/km^2)	One-σ error ($\pm10^{-2}$N/km^2)	Lower age limit (Ma)	Average age (Ma)	Higher age limit (Ma)	Surface (km^2)	TiO_2 (wt%)	FeO (wt%)	Original units (Ref. Fig. 10)
1a	6.8	1.0	3390	3500	3580	13,239	2.0	17.3	103, 104, 105
1b	6.2	1.0	3310	3430	3530	2929	2.2	17.5	78
1c	6.2	1.0	3310	3430	3530	1039	2.6	16.7	74
1d	5.3	0.9	2900	3330	3430	4964	2.4	15.1	69, 70, 71
1e	5.3	0.9	2900	3330	3430	3298	2.3	16.6	17, 18
2a	6.2	1.0	3310	3430	3530	17,732	1.8	19.3	1, 200, 25, 29, 33
2b	6.1	1.0	3300	3420	3520	8761	2.1	18.4	77, 79
2c	6.1	1.0	3300	3420	3520	385	2.6	18.9	95
2d	6.0	1.0	3280	3410	3510	1434	2.2	19.8	39, 40
2e	6.1	1.0	3300	3420	3520	2575	2.6	19.7	19, 20
2f	5.8	1.0	3160	3390	3500	751	2.7	19.1	44
2g	7.4	1.1	3450	3550	3610	1683	1.5	18.6	3
3a	5.8	1.0	3160	3390	3500	2404	2.8	20.4	102
3b	6.1	1.0	3300	3420	3520	1086	2.2	20.3	85
3c	5.6	0.9	3140	3360	3460	2777	2.9	20.2	84
3d	6.1	1.0	3300	3420	3520	676	2.6	19.9	35
3e	6.2	1.0	3310	3430	3530	1267	2.8	20.0	24
3f	6.0	1.0	3280	3410	3510	4218	2.8	20.6	14
3g	7.1	1.1	3410	3520	3600	6108	2.5	20.3	6
3h	6.8	1.0	3390	3500	3580	2355	2.8	20.2	9
4a	6.6	1.0	3360	3470	3560	1418	3.0	14.6	37
4b	6.4	1.0	3340	3450	3550	2321	3.1	17.4	73
4c	5.3	0.9	2900	3330	3430	7319	3.5	15.7	56
4d	5.3	0.9	2900	3330	3430	930	3.1	16.4	48
4e	5.1	0.9	2800	3300	3410	5402	3.3	17.0	45, 46, 50
5a	5.3	0.9	2900	3330	3430	28,126	3.5	19.7	99, 100, 101, 94, 91, 92
5b	5.5	0.9	3050	3350	3450	6021	3.0	19.4	34
5c	5.1	0.9	2800	3300	3410	2386	3.1	19.5	54
5d	5.3	0.9	2900	3330	3430	5010	3.4	19.8	23, 28
5e	6.9	1.1	3400	3510	3590	1748	3.6	19.8	12
5f	6.0	1.0	3280	3410	3510	1516	3.1	19.0	88
6a	4.8	0.9	2575	3160	3370	1745	3.1	20.4	101
6b	5.3	0.9	2900	3330	3430	4949	3.3	19.9	90
6c	5.3	0.9	2900	3330	3430	1801	3.6	20.3	80, 82
6d	4.8	0.9	2575	3160	3370	1169	3.0	20.2	36
6e	4.7	0.9	2560	3140	3360	1528	3.3	20.8	27
6f	4.8	0.9	2575	3160	3370	5926	3.4	20.5	21
6g	7.4	1.1	3450	3550	3610	11,787	3.6	20.8	16
6h	4.8	0.9	2575	3160	3370	81,656	3.4	20.3	7, 107, 2
7a	4.7	0.9	2560	3140	3360	2253	4.0	17.7	62
8a	4.7	0.9	2560	3140	3360	10,415	3.9	18.2	72
8b	4.7	0.9	2560	3140	3360	11,140	4.0	18.3	51, 52
8c	4.5	0.8	2500	2970	3330	1185	3.9	19.7	97, 98
9a	3.5	0.7	1900	2340	2800	57,860	4.3	20.5	57, 61, 59, 32, 30, 31, 86,
9b	4.6	0.9	2500	3050	3350	8528	3.9	21.3	10, 11, 13
9c	3.8	0.8	2000	2560	3050	1989	4.4	21.9	15
9d	6.4	1.0	3340	3450	3550	745	4.6	21.4	4
9e	3.8	0.8	2000	2560	3050	11,296	4.8	21.3	83, 89, 106

Table 5. Grouped units from Table 4 with similar chemical compositions and inferred ages.

Groups	TiO_2 (wt%)	FeO (wt%)	Units (Ref. Table 4)	Surface (km^2)	Sample crater count ($10^{-2}N/km^2$)	Age (Ma)
1	2.1	17.2	1a, 1c	14,278	6.8	3500
2	2.1	19.5	2g, 3g	7791	7.2	3530
3	2.2	17.5	1b	2929	6.2	3430
4	2.2	19.4	2a, 2b, 2d, 2e, 3b, 3e, 3f, 3h	39,428	6.2	3430
5	2.4	15.7	1d, 1e	8262	5.3	3330
6	2.7	19.8	2c, 2f, 3a, 3c, 3d	6993	5.8	3390
7	3.1	16.2	4a, 4b	3739	6.5	3460
8	3.2	20.3	6a, 6b, 6d, 6e	9391	5.0	3280
9	3.4	19.8	6f, 5b, 5c, 5d, 5f	20,859	5.2	3320
10	3.4	16.3	4c, 4d, 4e	13,651	5.2	3320
11	3.4	20.3	6h	81,656	4.8	3160
12	3.6	20.4	5e, 6g	13,535	7.3	3540
13	3.7	20.9	5a, 6c, 9b	38,455	5.3	3330
14	4.0	18.3	7a, 8a, 8b, 8c	24,993	4.7	3140
15	4.3	20.5	9a	57,860	3.5	2340
16	4.6	21.4	9d	745	6.4	3450
17	4.7	21.4	9c, 9e	13,285	3.8	2560

Table 6. Further merging and subgrouping of the 17 groups from Table 5 into eight potential geological types.

Family	Groups (new)	TiO_2 (wt%)	FeO (wt%)	Crater count ($10^{-2}N/km^2$)	Age (Ma)	Surface (km^2)	Original groups (Ref. Table 5)
I	a	2.1	18.1	6.8	3500	24,998	1, 2, 3
	b	2.2	19.4	6.2	3430	39,428	4
	c	2.7	19.8	5.8	3390	6990	6
II	d	3.5	19.0	5.3	3330	72,965	9, 10, 13
	e	3.3	20.3	4.9	3270	91,047	8, 11
	f	4.0	18.3	4.7	3140	24,993	14
III	g	4.7	21.4	3.8	2560	13,285	17
	h	4.3	20.5	3.5	2340	57,860	15
Subfamily							
IV	d	3.6	20.4	7.3	3540	13,535	12
V	g	4.6	21.4	6.4	3450	745	16
VI	b	3.1	16.2	6.5	3460	3739	7
VII	a	2.4	15.7	5.3	3330	8265	5

Mauro). The largest example of this type of terrain crops out east of Rupes Recta. Although it is virtually indistinguishable in optical images from the rest of the neighboring mare west of the unit (including albedo characteristics), our spectral analysis indicates a composition (FeO and TiO_2) very similar and comparable to the highlands to the east ("y" in Fig. 19). We believe that this area might have been relatively unaffected by later maria flows by virtue of its elevated topography. Its "red" color might reflect the inherent properties of the basalts, with contributions from the west as bedrock material excavated and ejected by the Birt impact, from the south as terra material transported by the Tycho blast, and from below as excavated bedrock material. We date these maria as Imbrian in age (~3.8 Ga).

Patches of ancient maria (Ia) can also be found scattered around the periphery of the basins or infilling ancient crater floors. Examples are the bay next to Davy and Alphonsus, (unit 79 from Fig. 10), east of Mosting (104), northeastern Mare Cognitum (3), next to Montes Riphaeus (6), and within the craters Pitatus (71) and Mercator (18). All these areas either border or are enclosed by terra. Contamination and mass movement contributed partially to the enhanced affinity in mineralogy of the constituent basalts with highland materials (lower than average FeO and TiO_2). Also significant could be the inclusion of bedrock material excavated by impacts in these shallow maria.

The remnant units belonging to group I feature some of the most distinctive basalt flows on the lunar surface. In particular, the terrain stretching south from the western side of the Fra Mauro peninsula to the Nicollet crater in Eastern Nubium is detectable even on relatively low-resolution Earth-based images of the Moon. It clearly stands out from the darker maria with rather well-defined borders. Closer inspection reveals a highly cratered surface, with relatively

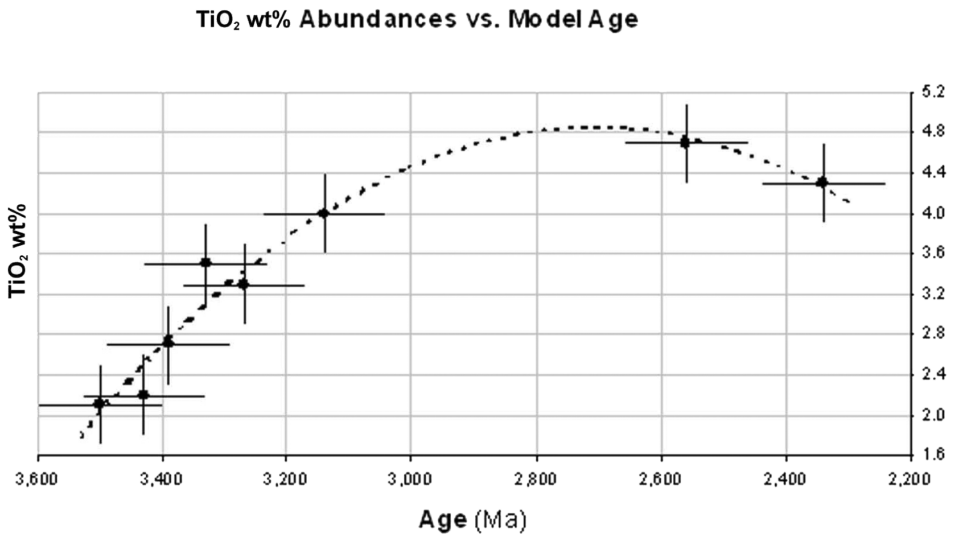

Fig. 16. A graph of TiO_2 wt% abundances versus model age.

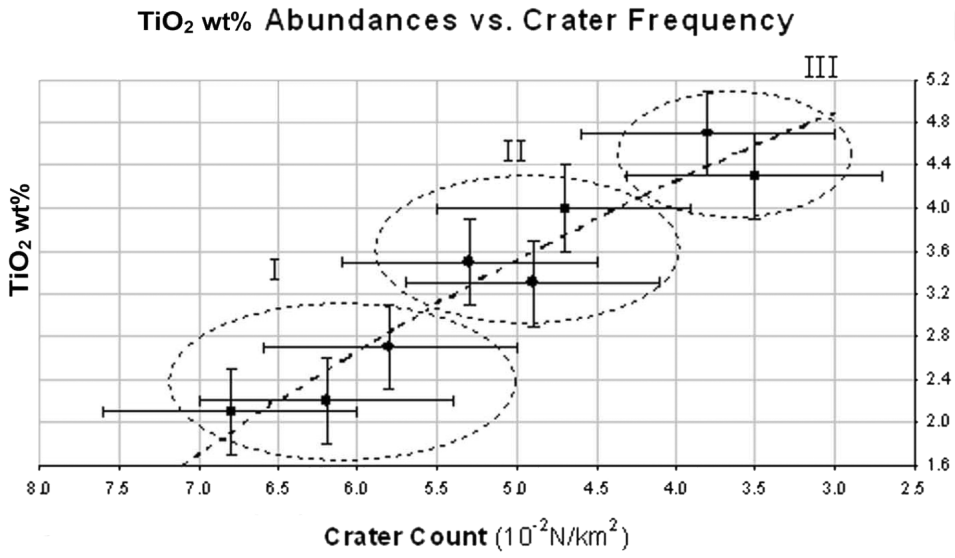

Fig. 17. A graph of TiO_2 wt% abundances versus crater frequency.

low titanium content but nearly average mare iron signature. Indeed, the TiO_2 content in the regolith of units 1, 25, and 29 is comparable to that in the nearby highlands (Fra Mauro and south of Guericke).

Both the high crater count and chemical signature point toward a relatively old age for these terrains (Upper Imbrian Series) and relatively shallow depths. Also note how some areas of these units have been subsequently mantled over by later flows (Ic, 84) or presumably, a series of basalt units (from IId, 34, up to IIIh, 61).

Most of the northern and eastern parts of the region (around 15°S, 20°W) are covered by basaltic material belonging to the early Eratosthenian Period. Within Nubium, ejecta from the Bullialdus crater (61 km in diameter) and associated secondary craters have rearranged and masked most of the pre-existing terrains in the western Nubium basin. Only small patches of Imbrian-age material are visible (Ib, 24, 20, and 39–40). Following the impact event, subsequent basaltic flows covered some of the ejecta itself. Most apparent is the IId maria east of Lubiniezky (20). The iron content that

Table 7. Proposed three major eruptive phases in the Nubium/Cognitum region.

Family	TiO_2 (wt%)	FeO (wt%)	Start–End (Ga)
I	2.0–3.0	18.0–20.0	3.4 ± 0.1
II	3.0–4.0	18.0–20.5	3.2 ± 0.1
III	4.0–5.0	20.0–21.5	2.7 ± 0.4

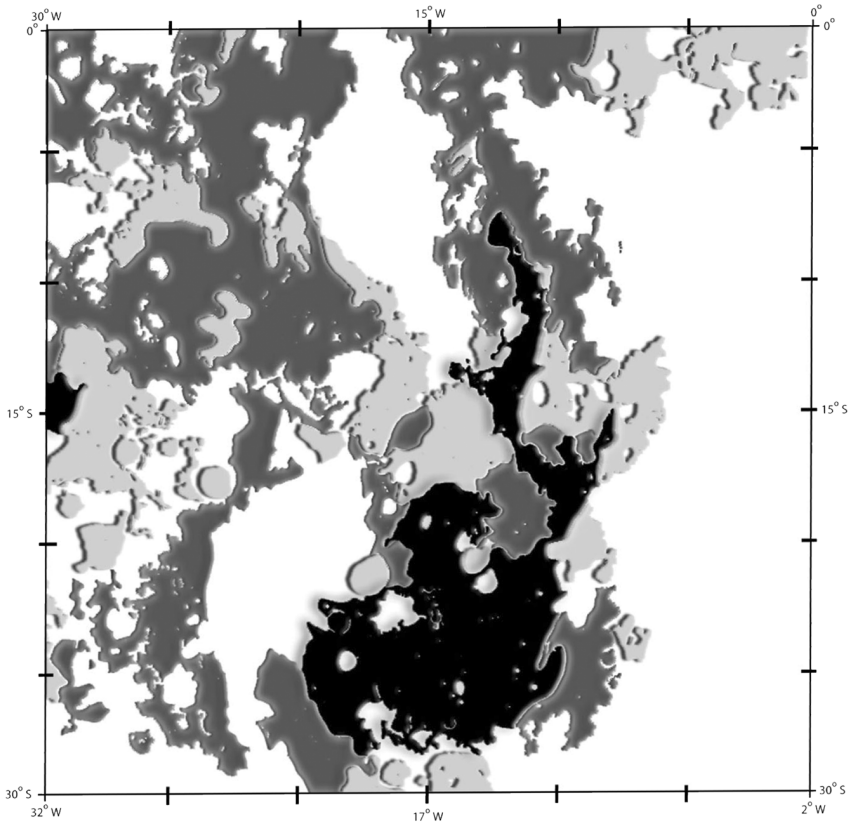

Fig. 18. A map showing the three major eruptive phases in Mare Nubium (darker = younger; white is upland or crater ejecta materials).

is higher than the underlying crater material (21) betrays its presence.

Mare Cognitum shows an intricate pattern of flow units. Old Imbrian basalts are confined to mare close to Montes Riphaeus (6 and 9), further south of the mountains (14), and northeastern Mare Cognitum (3).

Most of the area is covered with regolith belonging to the IIe unit type, except for a large area south of the basin, which is dominated by older, more Ti-rich basalts (IId, 16, 10, 11, 12). We find soils of similar composition on the other side of the mountains (21), possibly belonging to related and contemporary mare flows. Similar regolith covers most of the mare corridor between Fra Mauro and the highlands in the east.

The last major maria flows (late Eratosthenian) were confined to large areas around the central Nubium basin. The titanium composite reveals a relatively high-Ti basaltic unit stretching for 400 km in a narrow flow on the eastern side of Fra Mauro (IIIg, 89, 83, 106). Similar mare material can also be found northeast of Mare Cognitum (4), a much more modest 745 km^2 flow that appears extremely smooth and dark in standard photography.

The largest single unit flow in the region occupies most of the central part of the Nubium basin (IIIh, 57, 61). The impact seismic energy and ejecta material from the much younger Tycho impact have reworked some of the regolith in the area. Nevertheless, both crater frequency and soil characteristics point to a massive outpouring of magmatic material late in the infill of the Nubium basin. Unfortunately, we cannot directly measure the depth of this latest emplacement and consequently cannot estimate the volume of the erupted lava. These flows appear to have infilled areas of lower topography, already with a relatively flat morphology. This could explain the large geographical distribution of even a relatively modest effusive phenomenon so late in the thermal history of the Moon.

CONCLUSIONS

Nine potential mare units are mapped and classified, each with its characteristic chemical composition (FeO and TiO_2 abundances) and age.

A correlation between flow composition and age was noted. Titanium content in the basalts appears to relate to the time of eruption, with a progressively higher amount in younger units. Iron displays a similar but weaker trend.

The exposed lava fields in the region suggest three distinct periods of effusion, each lasting around 300 Ma. The oldest exposed flows date back to the Late Imbrian Epoch (~3.4 ± 0.1 Ga), with TiO_2 content between 2–3 wt%. A

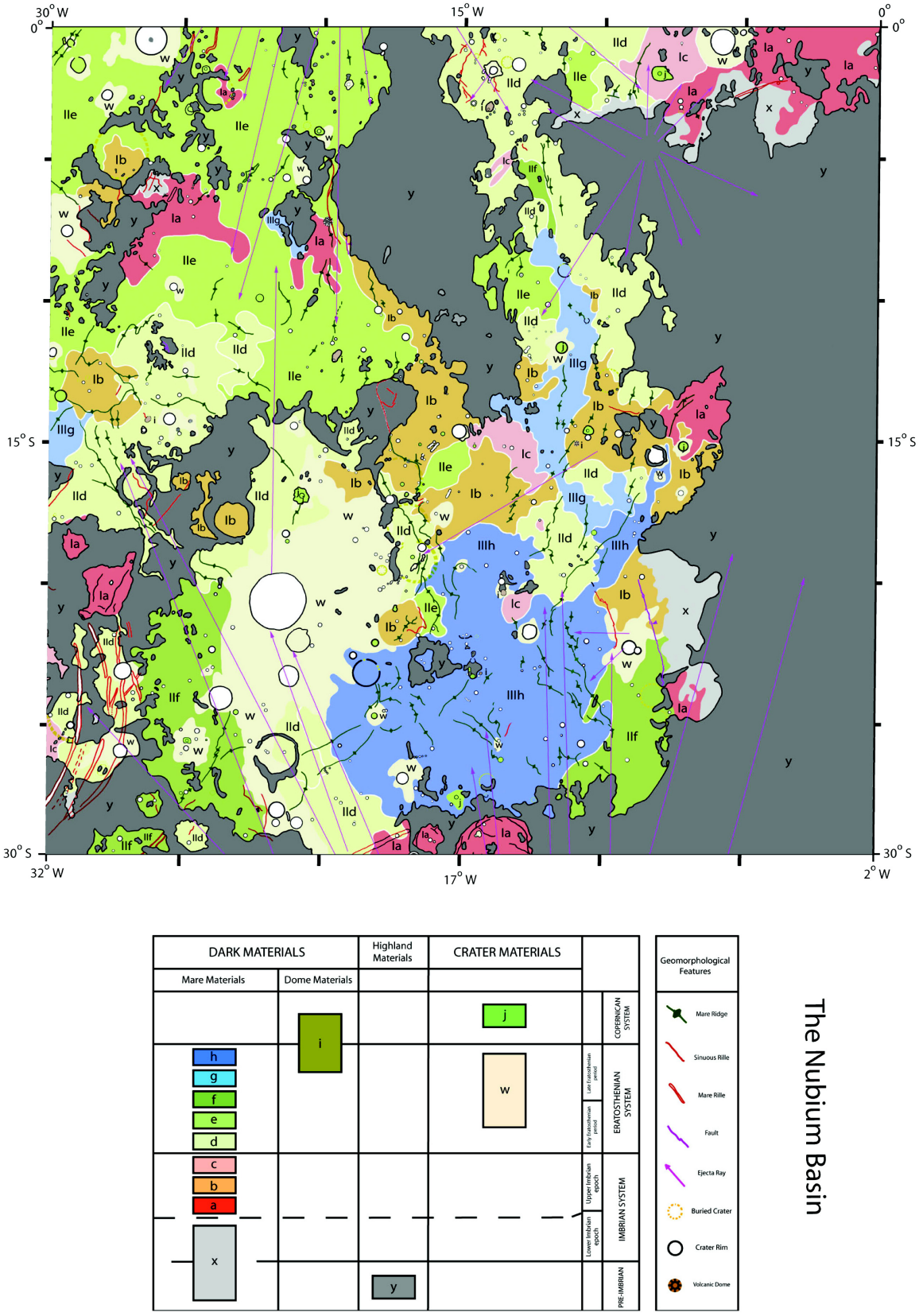

Fig. 19. A geologic map of the Mare Nubium and Mare Cognitum region.

shorter but more extensive effusive period followed, with basalts covering most of the region's lower topography (early Eratosthenian Period, ~3.2 ± 0.1 Ga, 3–4 wt% TiO_2). The last massive outpouring of lava continued until the late Eratosthenian Period; we have dated the youngest units at around 2.7 ± 0.4 Ga with TiO_2 content of 4–5 wt%.

Acknowledgments–We appreciate Brian Fessler at the Jet Propulsion Laboratory for his technical assistance and patience. We would also thank Dominique Fortes for his knowledgeable comments, suggestions and for his much-welcomed and fastidious proofreading.

Editorial Handling—Dr. Carlé Pieters

REFERENCES

Arvidson R. E., Drozd R., Guinness E., Hohenberg C., and Morgan C. 1976. Cosmic ray exposure ages of Apollo 17 samples and the age of Tycho. Proceedings, 7th Lunar Science Conference. pp. 2817–2832.

Belton J. S., Head J. W. III, Pieters C. M., Greeley R., McEwen A. S., Neukum G., Klaasen K. P., Anger C. D., Carr M. H., and Chapman C. R. 1992. Lunar impact basins and crustal heterogeneity—New western limb and far side data from Galileo. *Science* 255:570–576.

Blewett D. T., Lucey P. G., Hawke B. R., and Jolliff B. L. 1997. Clementine images of the lunar sample-return stations: Refinement of FeO and TiO_2 mapping techniques. *Journal of Geophysical Research* 102:16,319–16,326.

Blewett D. T. and Hawke B. R. 2001. Remote sensing and geological studies of the Hadley-Apennine region of the Moon. *Meteoritics & Planetary Science* 36:701–730.

Boyce J. M. 1975. Chronology of flow units in western maria. *Conference on origins of mare basalts and their implications for lunar evolution*. Houston: Lunar Science Institute. pp. 12–15.

Budney C. J. and Lucey P. G. 1998. Basalt thickness in Mare Humorum: The crater excavation method. *Journal of Geophysical Research* 103:16,855–16,870.

Basaltic Volcanism Study Project. 1981. *Basaltic volcanism on the terrestrial planets*. New York: Pergamon Press. 1286 p.

Campbell B. A., Hawke B. R., and Thompson T. W. 1997. Regolith composition and structure in the lunar maria: Results of long-wavelength radar studies. *Journal of Geophysical Research* 102: 19,307–19,3200.s

Charette M. P., McCord T. B., Pieters C., and Adams J. B. 1974. Application of remote spectral reflectance measurements to lunar geology classification and determination of titanium content of lunar soils. *Journal of Geophysical Research* 79:1605–1613.

de Hon R. A. 1977. Mare Humorum and Mare Nubium: Basalt thickness and basin-forming history. Proceedings, 8th Lunar Science Conference. pp. 633–641.

Eliason E. M. 1997. Production of digital image models using the ISIS system. 28th Lunar and Planetary Science Conference. pp. 331–332.

Eliason E. M., Malaret E. R., and Woodward G. 1995. Clementine Mission: The Archive of image data products and data processing capabilities. 26th Lunar and Planetary Science Conference. pp. 369–370.

Eliason E. M, Isbell C., Lee E. M., Becker T., and Gaddis L. R. 1999. The Clementine UVVIS global lunar mosaic. U.S. Geological Survey. Astrogeology Team, 2255 North Gemini Drive. Flagstaff, Arizona 86001, USA.

Elphic R. C., Lawrence D. J., Maurice S., Feldman W. C., Barraclough B. L., Gasnault O. M., Lucey P. G., Blewett D. T., and Binder A. B. 2001. Lunar Prospector neutron measurements and TiO_2 in mare basalt soils (abstract #P21A-06). Proceedings, American Geophysical Union Spring Meeting 2001.

Fisher E. M., Pieters C. M, and Pratt S. P. 1994. Modelling the space weathering–induced optical alteration of lunar soils: First results. 25th Lunar and Planetary Science Conference. pp. 371–372.

Fisher E. M. and Pieters C. M. 1996. Composition and exposure age of the Apollo 16 Cayley and Descartes regions from Clementine data: Normalizing the optical effects of space weathering. *Journal of Geophysical Research* 101:2225–2234.

Giguere T. A., Taylor G. J., Hawke B. R., and Lucey P. G. 2000. The titanium contents of lunar mare basalts. *Metoritics & Planetary Science* 35:193–200.

Gault D. E., Hörtz F., Brownlee D. E., and Hartung J. B. 1974. Mixing of the lunar regolith. Proceedings, 5th Lunar Science Conference. pp. 2365–2386.

Gillis J. J. and Jolliff B. L. 2001. Bimodal TiO_2 contents of mare basalts at Apollo and Luna sites and implications for TiO_2 derived from Clementine spectral reflectance (abstract #2164). 32nd Lunar and Planetary Science Conference. CD-ROM.

Gillis J. J., Jolliff B. L., and Elphic R. C. 2003. A revised algorithm for calculating TiO_2 from Clementine UVVIS data: A synthesis of rock, soil, and remotely sensed TiO_2 concentrations. *Journal of Geophysical Research* 108:3-1–3-18.

Gillis J. J., Lucey P. G., and Lawrence S. J. 2004. Testing the relation between UVVIS color and TiO_2 composition in the lunar maria (abstract # 1840). 35th Lunar and Planetary Science Conference. CD-ROM.

Grieve R. A. F. and Pilkington M. 1996. The signature of terrestrial impacts. *AGSO Journal of Australian Geology and Geophysics* 16:399–420.

Hall A. 1996. *Igneous petrology*, 2nd edition. Harlow, England: Longman Group Limited. 550 p.

Hapke B., Danielson G. E., Klaasen K., and Wilson L. 1975. Photometric observations of Mercury from Mariner 10. *Journal of Geophysical Research* 80:2431–2443.

Hawke B. R. and Head J. W. 1977. Pre-Imbrian history of the Fra Mauro region and Apollo 14 sample provenance. Proceedings, 8th Lunar Science Conference. pp. 2741–2761.

Hawke B. R., Gillis J. J., Giguere T. A., Blewett D. T., Lawrence D. J., Lucey P. G., Peterson C. A., Smith G. A., Smith G. A., Spudis G. A., and Taylor G. J. 2005. The earliest mare basalts (abstract #1642). 36th Lunar and Planetary Science Conference. CD-ROM.

Heiken G. 1975. Petrology of lunar soils. *Reviews of Geophysics and Space Physics* 13:567–587.

Hiesinger H., Jaumann R., Neukum G., and Head J. H. III. 2000. Ages of mare basalts on the lunar nearside. *Journal of Geophysical Research* 105:29,239– 29,275.

Hiesinger H., Jaumann R., Neukum G., and Head J. H. III. 2001. Ages and mineralogical variation of lunar mare basalts (abstract #P21A-04). Proceedings, American Geophysical Union Spring Meeting 2001.

Hiesinger H., Head J. W., Wolf U., Jaumann R., and Neukum G. 2003. Ages and stratigraphy of mare basalts in Oceanus Procellarum, Mare Nubium, Mare Cognitum, and Mare Insularum. *Journal of Geophysical Research,* doi:10.1029/2002JE001985.

Hörz F. 1978. How thick are lunar mare basalts? Proceedings, 9th Lunar and Planetary Science Conference. pp. 3311–3331.

Hörz F., Grieve R., Heiken G., Spudis P. D, and Binder A. 1991.

Lunar surface processes. In *Lunar sourcebook: A user's guide to the Moon*. New York: Cambridge University Press. 736 p.

Houck K. J. 1982. Petrologic variations in Apollo 16 surface soils. Proceedings, 13th Lunar and Planetary Science Conference. pp. A197–A209.

Housley R. M. 1980. Toward a model of grain surface exposure in planetary regoliths. In *The ancient sun: Fossil record in the Earth, Moon and meteorites*. Oxford: Pergamon Press. pp. 401–410.

Isbell C. E., Eliason E. M., Adams K. C., Becker T. L., Bennett A. L., Lee E. M., McEwen A. S., Robinson M. S., Shinaman J. R., and Weller L. A. 1999. Clementine: A multispectral digital image model archive of the Moon (abstract #1812). 30th Lunar Planetary Science Conference. CD-ROM.

Johnson T. V., Saunders R. S., Matson D. L., and Mosher J. A. 1977. A TiO_2 abundance map for the northern maria. 8th Lunar Science Conference. pp. 1029–1036.

Johnson P. E., Smith M. O., and Adams J. B. 1985. Quantitative analysis of planetary reflectance spectra with principal component analysis. Proceedings, 15th Lunar and Planetary Science Conference. pp. C805–C810.

Johnson J. R., Larson S. M., and Singer R. B. 1991. Remote sensing of potential lunar resources 1. Near-side compositional properties. *Journal of Geophysical Research* 96:18,861–18,882.

Jolliff B. L, Gaddis L. R., Ryder G., Neal C. R., Shearer C. K., Elphic R. C., Johnson J. R., Keller L. P., Korotev, R. L., Lawrence D. J., Lucey P. G., Papike J. J., Pieters C. M., Spudis P. D., and Taylor L. A. 2000. New views of the Moon: Improved understanding through data integration. *EOS Transactions* 81:354–355.

Keller L. P., Wentworth S. J., and McKay D. S. 1998. Space weathering: Reflectance spectroscopy and TEM analysis of individual lunar soil grains. 29th Lunar and Planetary Science Conference (abstract #1762). CD-ROM.

Keller L. P, Wentworth S. J., Gezo J., McKay D. S., Taylor L. A., Pieters C., and Morris R. V. 1999. Space weathering alteration of lunar soil grains (abstract #1820). 30th Lunar and Planetary Science Conference. CD-ROM.

Keller L. P., Wentworth S. J., McKay D. S., Taylor L. A., Pieters C., and Morris R. V. 2000. Space weathering in the fine size fraction of lunar soils: Mare/highland differences (abstract #1655). 31st Lunar and Planetary Science Conference. CD-ROM.

Kuiper G. P., Whitaker E. A., Strom R. G., Fountain J. W., and Larson S. M. 1967. *Consolidated lunar atlas*. Tucson: The University of Arizona Press.

Kreslavsky M. A., Shkuratov Yu. G., Velikodsky Yu. I., Kaydash V. G., and Stankevich D. G. 2000. Photometric properties of the lunar surface derived from Clementine observations. *Journal of Geophysical Research* 105:20,281– 20,295.

Langevin Y. and Arnold J. R. 1977. The evolution of the lunar regolith. *Annual Reviews of Earth and Planetary Science* 5:449–489.

Li L. and Mustard J. F. 2000. The compositional gradients and lateral transport by dark-halo and dark-ray craters (abstract #2007). 31st Lunar and Planetary Science Conference. CD-ROM.

Lucey P. G., Taylor G. J., and Malaret E. 1995. Abundance and distribution of iron on the Moon. *Science* 268:1150–1153.

Lucey P. G., Blewett D. T., Johnson J. R., Taylor G. J., and Hawke B. R.1996. Lunar titanium content from UV-VIS measurements. 25th Lunar and Planetary Science Conference. pp. 781–782.

Lucey P. G., Blewett D. T., and Hawke B. R. 1998. Mapping the FeO and TiO_2 content of the lunar surface with multispectral imagery. *Journal of Geophysical Research* 103:3679–3699.

Lucey P. G., Blewett D. T., and Jolliff B. L. 2000a. Lunar iron and titanium abundances algorithms based on final processing of Clementine ultraviolet-visible images. J*ournal of Geophysical Research* 105:20,297–20,305.

Lucey P. G., Bewett D. T., Taylor G. J., and Hawke B. R. 2000. Imaging of lunar surface maturity. *Journal of Geophysical Research* 105:20,377–20,386.

Matson D. L., Johnson T. V., and Veeder G. J. 1977. Soil maturity and planetary regoliths: The Moon, Mercury, and the asteroids. Proceedings, 8th Lunar Science Conference. pp. 1001–1012.

McCord T. B. and Adams J. B. 1973. Progress in optical analysis of lunar surface composition. *The Moon* 7:453–474.

McKay D. S., Heiken G., Basu A., Blanford G., Simon S., Reedy R., and French B. M. 1991. The lunar regolith. In *Lunar sourcebook: A user's guide to the Moon*. New York: Cambridge University Press. 736 p.

Melendrez D. E., Johnson J. R., Larson S. M., and Singer R. B. 1994. Remote sensing of potential lunar resource 2: High spatial resolution mapping of spectral reflectance ratios and implications for nearside mare TiO_2 content. *Journal of Geophysical Research* 99:5,601–5,620.

Melosh H. J. 1989. *Impact cratering: A geologic process*. New York: Oxford University Press. 245 p.

Moore H. J., Boyce J. M., Schaber G. G., and Scott D. H. 1980. Lunar remote sensing and measurements. USGS professional paper #1046-B. Washington, D.C.: U.S. Geological Survey.

Mustard J. F. and Head J. W. 1996. Buried stratigraphic relationships along the southwestern shores of Oceanus Procellarum: Implications for early lunar volcanism. *Journal of Geophysical Research* 101:18,913–18,926.

Mysen B. O. and Kushiro I. 1977. Compositional variations of coexisting phases with degree of melting of peridotite in the upper mantle. *American Mineralogist* 62:843–65.

Neukum G., Koenig B., and Arkani-Hamed J. 1975a. A study of lunar impact crater size-distributions. *The Moon* 12:201–229.

Noble S. K., Pieters C., Taylor L. A., Morris R. V., Allen C. C., McKay D. S, and Keller L. P. 2000. Optical properties of the finest fractions of lunar soil: Implications for space weathering environments (abstract #1810). 31st Lunar and Planetary Science Conference. CD-ROM.

Nozette S., Lewis I. T., Lichtenberg C. L., Lucey P. G., Malaret E., Massie M. A., Resnick J. H., Rollins C. J., Park H. S., McEwen A. S., Priest R. E., Pieters C. M., Reisse R. A., Robinson M. S., Simpson R. A., Smith D. E., Sorenson T. C., Bruegge R., Vorder W., and Zuber M. T. 1994. The Clementine Mission to the Moon: Scientific overview. *Science* 266:1835–1839.

Oberbeck V. R., Quaid W. L., Mahan M., and Paulson S. 1973. Monte Carlo calculations of lunar regolith, thickness, and distribution. *Icarus* 19:87–107.

Papike J., Taylor L., and Simon S. 1991. Lunar minerals. In *Lunar sourcebook: A user's guide to the Moon*. New York: Cambridge University Press. 736 p.

Pieters C. M. 1978. Mare basalts on the front side of the moon: A summary of spectral reflectance data. Proceedings, 9th Lunar Planetary Science Conference. pp. 2825–2849.

Pieters C. M. and McCord 1976. Characterization of lunar mare basalt types. I. A remote sensing study using reflection spectroscopy of surface soils. Proceedings, 7th Lunar Science Conference. pp. 2677–2690.

Pieters C. M., Sunshine J. M., Fischer E. M., Murchie S. L., Belton M., McEwen A., Gaddis L., Greeley R., Neukum G., Jaumann R., and Hoffmann H. 1993. Crustal diversity of the Moon: Compositional analyses of Galileo SSI data. *Journal of Geophysical Research* 98:17,127–17,148.

Pieters C. M., Staid M. I., Fischer E. M., Tompkins S., and He G. 1994. A sharper view of impact craters from Clementine data. *Science* 266:1844–1848.

Pike R. J. 1974. Depth/diameter relations of fresh impact craters: Revision from spacecraft data. *Geophysical Research Letters* 1: 291–294.

Rhodes J. M. 1977. *Philosophical Transactions of the Royal Society of London A* 285:293–301.

Robinson M. S., McEwen A. S., Eliason E., Lee E. M., Malaret E., and Lucey P. G. 1999. Clementine UV-VIS global mosaic: A new tool for understanding the lunar crust (abstract #1931). 30th Lunar and Planetary Science Conference. CD-ROM.

Shkuratov Y. G., Kaydash V. G., and Opanasenko N. V. 1999. Iron and titanium abundance and maturity degree distribution on the lunar nearside. *Icarus* 137:222–234.

Shoemaker E. M. 1977. Why study impact craters? In *Impact and explosion cratering: Planetary and terrestrial implications*, edited by Roddy D. J., Pepin R. O., and Merrill R. B. New York: Pergamon Press. pp.1–10.

Schultz P. H. and Spudis P. D. 1983. Beginning and end of lunar mare volcanism. *Nature* 302:233–236.

Spudis P. D. 1993. Geology multi-ring basins. New York: Cambridge University Press. 263 p.

Staid M. I., Pieters C. M., and Head J. W. 1996. Mare Tranquillitatis: Basalt emplacement history and relation to lunar samples. *Journal of Geophysical Research* 101:23,213–23,228.

Staid M. I. and Pieters C. M. 2000. Integrated spectral analysis of mare soils and craters: Applications to eastern nearside basalts. *Icarus* 145:122–139.

Staid M. I. and Pieters C. M. 2001. Mineralogy of the last lunar basalts: Results from Clementine. *Journal of Geophysical Research* 106:27,887–27,900.

Stöffler D., Gault E. E., Wedekind J., and Polkowski G. 1975. Experimental hypervelocity impact into quartz sand: Distribution and shock metamorphism of ejecta. *Journal of Geophysical Research* 80:4062–4077.

Stuart-Alexandra D. E. and Howard K. A. 1970. Lunar maria and circular basins—A review. *Icarus* 12:440–456.

Taylor S. R. 1975. *Lunar science: A post-Apollo view*. New York: Pergamon Press. 372 p.

Taylor S. R. 1982. Planetary science: A lunar perspective. Houston: Lunar and Planetary Institute. 481 p.

Thomson B. J., Spudis P. D., and Bussey D. B. 1998. Impact craters as probes of the lunar crust (abstract #1820). 29th Lunar and Planetary Science. CD-ROM.

Torson J. M. and K. J. Becker. 1977. ISIS—A software architecture for processing planetary images. 28th Lunar and Planetary Science Conference. pp. 1443–1444.

Whitaker E. A. 1972a. Colour contrasts in Mare Nubium and the Southern Oceanus Procellarum. Apollo 16 Preliminary Science Report, NASA Manned Spacecraft Centre. pp. 104–105.

Whitaker E. A. 1972b. Lunar color boundaries and their relationship to topographic features: A preliminary survey. *The Moon* 4:523–530.

Wilhelms D. E. and J. F. McCauley. 1971. Geologic map of the near side of the Moon. USGS #I-703. Washington, D.C.: U.S. Geological Survey.